Hindawi
Advances in Materials Science and Engineering
Volume 2019, Article ID 9628142, 13 pages
https://doi.org/10.1155/2019/9628142

Research Article

A Case Study on the Control of Large Deformations in a Roadway Located in the Du'erping Coal Mine in China

Xiaojie Yang,[1,2] Chaowen Hu,[1,2] Jianhui Liang,[3] Yubo Zhou,[2] Guofeng Ni,[3] and Ruifeng Huang[1,2]

[1]*State Key Laboratory for GeoMechanics and Deep Underground Engineering, China University of Mining and Technology, Beijing 100083, China*
[2]*School of Mechanic and Civil Engineering, China University of Mining and Technology, Beijing 100083, China*
[3]*Du'erping Coal Mine, XiShan Coal Electricity Group Co., Ltd., Taiyuan, China*

Correspondence should be addressed to Chaowen Hu; 916167981@qq.com

Received 22 July 2018; Accepted 13 March 2019; Published 28 April 2019

Academic Editor: Fernando Lusquiños

The effective control of large roadway deformations has always been a focus and difficulty in the coal industry. At present, a "bolt + cable + mesh + shotcrete" combined support structure has been widely used in China to support roadways with large deformations, and this method has achieved some success. However, large roadway deformations supported by using the "bolt + cable + mesh + shotcrete" support structure still have a series of engineering problems. This paper describes a case study of large deformation control in a roadway surrounded with broken rock located in the Du'erping coal mine in the Shanxi Province of China. A new "shell + bolt + shotcrete" combined support structure is proposed to support the north wing main haulage roadway. Methods were adopted from theoretical analysis, numerical simulation, and similarity simulation experiments to design a reinforced shell within a vertical wall semicircular arch. Roadway convergence and surrounding rock stress were monitored on the site. The monitoring data showed that the new support structure successfully controlled a potentially large deformation of the roadway. This new combined support structure provides a helpful reference for the design and engineering of support structures to prevent large roadway deformations.

1. Engineering Background

As mining depths increase, engineers are finding more rock masses that show the characteristics of soft rock under the influence of high ground stress [1–5]. Increasingly, coal mining enterprises are being faced with the problem of how to support roadways that may contain large deformations. "Bolt + cable + mesh + shotcrete" combined support structures have usually been proposed to support roadways with large deformations in China, and this support method has been somewhat successful [7–10]. However, a roadway supported by using a "bolt + cable + mesh + shotcrete" structure is still vulnerable to instability or even failure. Roadway damage is serious and requires repeated repairs, which not only consumes human and material resources but also seriously affects coal mine safety [11–15].

As shown in Figure 1(a), the Du'erping coal mine (XiShan Coal Electricity Group Co., Ltd.) is located in Taiyuan city in China's Shanxi province. The north wing haulage roadway of the Du'erping coal mine is one of the more highly used roadways at the site. In this roadway, there exists a fracture zone that measures approximately 100 m in length between the North-4 and the North-5 roadway, as shown in Figure 1(b). As seen in Figure 2, the original support structure consisted of a "bolt + mesh + shotcrete" structure, but under the influence of high ground stress and mining activities, the portion of the roadway that contained the fracture zone became seriously deformed. The size of the

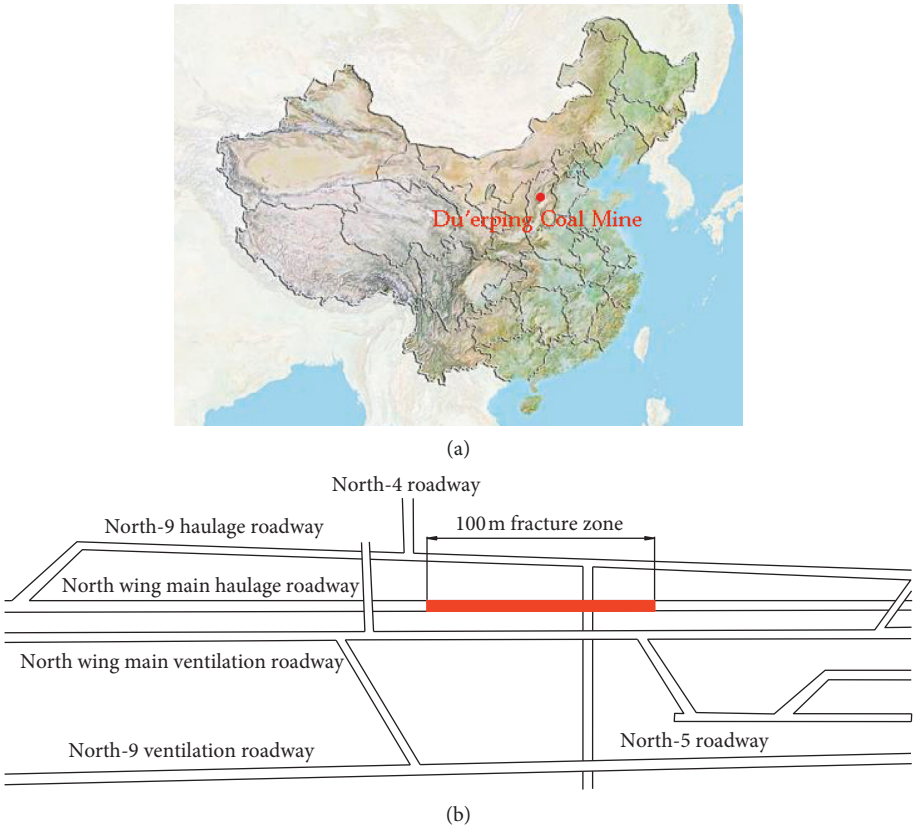

Figure 1: (a) Location of the Du'erping coal mine. Shanxi, China. (b) Location of the fracture zone in the north wing of the main haulage roadway.

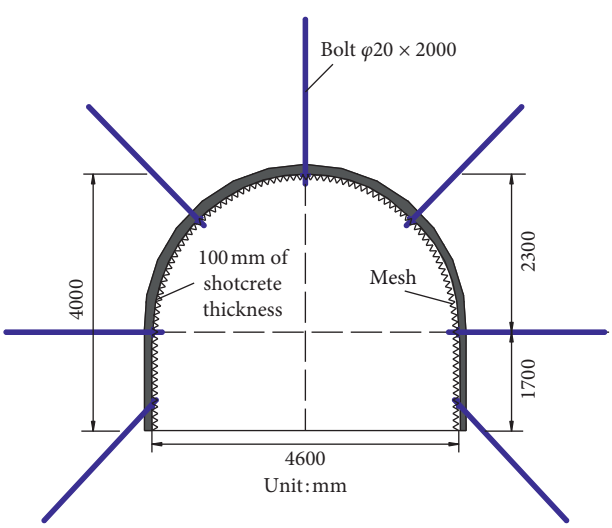

Figure 2: Original support structure.

roadway in this section was reduced from 4.6 m × 4.0 m to 3.5 m × 3.0 m. Although repaired many times, the repairs did not effectively reduce the deformation in the roadway. A new "shell + bolt + shotcrete" structure was proposed that was inspired by a long span shell structure [16–19], and this was combined with the existing support structure to support the fracture zone.

2. Theoretical Analysis of the New Support Structure

2.1. Principle of the New Support Structure. The new support structure is a "shell + bolt + shotcrete" combined support structure, and its support system is able to achieve both internal reinforcement and external support. The shell consists of arched steel bars and circular steel bars, and they are arched in both longitudinal and transverse directions, forming a space shell structure as a whole. The reticulated shell forms the skeleton, and the shotcrete forms a thin-walled reinforced concrete shell. The steel mesh shell concrete retaining structure draws on the superior mechanical properties of the shell structure and changes the ordinary "bolt + mesh + shotcrete" support structure into a space steel shell structure. The concrete spray layer is more evenly stressed, and its bearing capacity is increased. The new support system has both flexible and rigid support. Therefore, this support structure can effectively reduce roadway deformation in the surrounding broken rock.

The composition of the new support structure is shown in Figure 3. First, the bolts were arranged in a circle and installed in the surrounding rock of the roadway to form a range of reinforcement. Second, a plurality of components was assembled into a reinforced shell support and fixed on the surface of the surrounding rock to form an external support skeleton. Finally, shotcrete was installed to form an

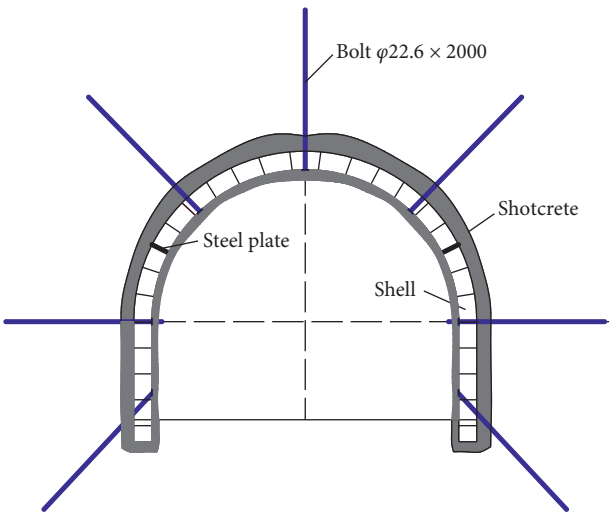

Figure 3: Structure of the new support structure.

entire support system. The shotcrete was installed in its colloidal form in the initial stage to not only close the internal fracture in the surrounding rock but also to deform with the surrounding rock and prevent a fracture [20–23]. The strength of the shotcrete was later increased, and it formed a lining structure that reinforced the shell support. The characteristics of the new support structure allowed the surrounding rock of the roadway to deform appropriately, thereby releasing the elastic energy of the surrounding rock, and avoid a sudden release of energy, which would cause roadway instability. The support structure provides high strength to support the surrounding rock, allows for high ground stress, and limits a large deformation in the surrounding rock. The "shell + bolt + shotcrete" structure is a semirigid support system that provides flexible support during the initial stages but results in rigid roadway support.

The essence of the new support structure is that bolts reinforce the surrounding rock, and the shotcrete closes fractures in the surrounding rock. The bolts, shotcrete, and surrounding rock form a unified whole support structure called an external arch. When the surrounding rock tends to be stable, then the shotcrete grouts to the bottom of the roadway and the reinforced shell is used as a preliminary support on the inside of the external arch. Then the shotcrete grouts to the reinforced shell, and the shotcrete and reinforced shell form a unified whole support structure called an internal arch. The whole support system controls large roadway deformations.

2.2. Internal Force Calculation of the Reinforced Shell. The geometric graph of the curved surface of the reinforced shell is shown in Figure 4. The length of the cylindrical shell is 1, radius is a, thickness is h, and flare angle is f_0. Therefore,

$$\xi = \frac{x}{a}, \qquad \beta = \frac{h^2}{12a^2}. \tag{1}$$

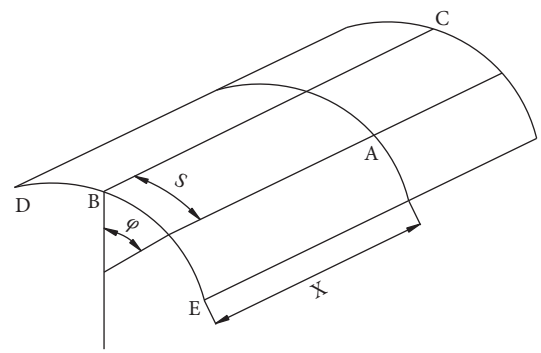

Figure 4: Geometric graph of the curved surface of the shell.

The basic equations of the cylindrical shell are expressed using a displacement component as follows:

$$\begin{cases} \dfrac{\partial^2 u}{\partial \xi^2} + \dfrac{1-\mu}{2}\dfrac{\partial^2 u}{\partial \psi^2} + \dfrac{1+\mu}{2}\dfrac{\partial^2 v}{\partial \xi \partial \psi} - \mu\dfrac{\partial w}{\partial \xi} = -\dfrac{(1-\mu^2)a^2 p_1}{Eh}, \\ \dfrac{1+\mu}{2}\dfrac{\partial^2 u}{\partial \xi \partial \psi} + \dfrac{1-\mu}{2}\dfrac{\partial^2 v}{\partial \xi^2} + \dfrac{\partial^2 v}{\partial \psi^2} - \dfrac{\partial w}{\partial \psi} = -\dfrac{(1-\mu^2)a^2 p_2}{Eh}, \\ \mu\dfrac{\partial u}{\partial \xi} + \dfrac{\partial v}{\partial \psi} - w - \beta\left(\dfrac{\partial^4 w}{\partial \xi^4} + 2\dfrac{\partial^4 w}{\partial \xi^2 \partial \psi^2} + \dfrac{\partial^4 w}{\partial \psi^4}\right) = -\dfrac{(1-\mu^2)a^2 p_3}{Eh}. \end{cases} \tag{2}$$

The internal force of the shell is shown in Figure 5. The equations for the internal force are simplified as follows:

$$\begin{cases} N_x = \dfrac{Eh}{1-\mu^2}\left[\dfrac{\partial u}{\partial x} + \mu\dfrac{1}{a}\left(\dfrac{\partial v}{\partial \psi} - w\right)\right], \\ N_\psi = \dfrac{Eh}{1-\mu^2}\left[\dfrac{1}{a}\left(\dfrac{\partial v}{\partial \psi} - w\right) + \mu\dfrac{\partial u}{\partial x}\right], \\ N_{x\psi} = \dfrac{Eh}{2(1+\mu)}\left(\dfrac{\partial v}{\partial x} + \dfrac{1}{a}\dfrac{\partial u}{\partial \psi}\right), \\ M_x = -D\left(\dfrac{\partial^2 w}{\partial x^2} + \mu\dfrac{1}{a^2}\dfrac{\partial^2 w}{\partial \psi^2}\right), \\ M_\psi = -D\left(\dfrac{1}{a^2}\dfrac{\partial^2 w}{\partial \psi^2} + \mu\dfrac{\partial^2 w}{\partial x^2}\right), \end{cases} \tag{3}$$

where $D = (Eh^3)/(12(1-\mu^2))$ is the flexural rigidity. The above equations can be simplified using an 8th partial differential equation, and the complete solution can be calculated using the following formula:

$$\nabla^2\nabla^2\nabla^2\nabla^2 F + \frac{1-\mu^2}{\beta}\frac{\partial^4 F}{\partial \xi^4} = \frac{a^4 p_3}{D}. \tag{4}$$

The homogeneous solution of equation (3) is the general solution of the following equation: $\nabla^2\nabla^2\nabla^2\nabla^2 F^0 + 4\alpha^4(\partial^4 F^0/\partial \xi^4) = 0$. The curved edges at both ends of the

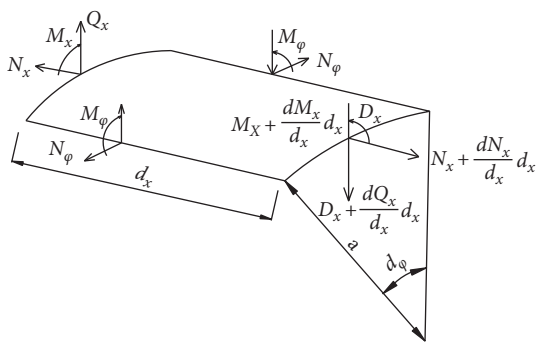

Figure 5: Internal force of the shell.

cylindrical shell are simply supported boundaries. Therefore, hypothetically, the formula for the solution is as follows: $\sum_{m=1}^{\infty} A_m e^{\eta\psi} \sin \lambda_m \xi$, where $\lambda_m = m\pi a/l$, where equations (1) and (2) are merged:

$$\sum_{m=1}^{\infty} \left\{ A_m \left[\left(\eta^2 - A_m^2 \right)^4 + 4\alpha^4 \lambda_m^4 \right] \right\} e^{\eta\psi} \sin \lambda_m \xi = 0, \tag{5}$$

where $e^{\eta\psi} \sin \lambda_m \xi \neq 0$ and $A_m \neq 0$, as obtained using equation (2); therefore,

$$\left(\eta^2 - A_m^2 \right)^4 + 4\alpha^4 \lambda_m^4 = 0. \tag{6}$$

The general solution of equation (4) can be simplified as follows:

$$\begin{aligned} F^0(\xi, \psi) = \sum_{m=1}^{\infty} \Big[& e^{-\rho a \psi} \left(B_1 e^{i\rho b \psi} + B_2 e^{-i\rho b \psi} \right) \\ & + e^{-\rho c \psi} \left(B_3 e^{i\rho d \psi} + B_4 e^{-i\rho d \psi} \right) \\ & + e^{\rho a \psi} \left(B_5 e^{i\rho b \psi} + B_6 e^{-i\rho b \psi} \right) \\ & + e^{-\rho c \psi} \left(B_7 e^{i\rho d \psi} + B_8 e^{-i\rho d \psi} \right) \Big] \sin \lambda_m \xi. \end{aligned} \tag{7}$$

The particular solution of equation (4) can be simplified using Euler's equation as follows:

$$F^*(\xi, \psi) = \sum_{m=1}^{\infty} q_m \varphi^* \sin \lambda_m \xi, \tag{8}$$

where $\varphi^* = \varphi^*(\psi)$ and q_m are the Fourier coefficients:

$$q_m = \frac{2}{\xi_0} \int_0^{\xi_0} p_3 \sin \lambda_m \xi \, d\xi. \tag{9}$$

The complete solution of equation (4) is the sum of equations (10) and (11) as follows:

$$F(\xi, \psi) = \sum_{m=1}^{\infty} \left(c_1 \varphi_1 + c_2 \varphi_2 + c_3 \varphi_3 + c_4 \varphi_4 + q_m \varphi^* \right) \sin \lambda_m \xi. \tag{10}$$

For the shell, the maximum value of basic stress can be obtained using the internal force directly as follows:

$$\begin{cases} \sigma_x = \dfrac{N_x}{h} + \dfrac{6M_x}{h^2}, \\ \sigma_\psi = \dfrac{N_\psi}{h} + \dfrac{6M_\psi}{h^2}, \\ \tau_{x\psi} = \tau_{\psi x} = \dfrac{N_{\psi x}}{h} + \dfrac{6M_{x\psi}}{h^2}. \end{cases} \tag{11}$$

According to the above formulas, the shell support can bear high ground stress and avoid stress concentration, and it is an effective support structure to control large deformations of the roadway.

3. Numerical Simulation

The support portion of the "shell + bolt + shotcrete" structure is a special reinforced concrete structure. ANSYS numerical simulation software was used to simulate the "shell + bolt + shotcrete" structure, which included investigations of the stress mechanism, failure process, evaluation of the ultimate bearing capacity, structural reliability, and analysis of feeble locations in the structure [24–27]. The results were used to optimize the structural design.

3.1. Numerical Model. The constitutive models used for the steel and concrete were the complete elastoplastic model and the elastoplastic model, respectively, and they are modeled using separate displacement coordination. Considering that the steel mesh shell support structure is symmetrical about the central axis of the roadway, and also to reduce the modeling workload and improve the analysis efficiency, only a half model was used to analyze and calculate the numerical simulation of the net shell member. Steel bar and concrete can both be modeled using an elastic-plastic model as their constitutive model. The parameters of the numerical model are shown in Table 1. The numerical model is shown in Figure 6.

3.2. Loading and Solving. Full constraints were applied on the top and bottom surface of the model. In addition, the Z-axis displacement constraints were applied to the lateral boundaries of the model, and surface loads were applied on the outside surface of the model. Deformation of the model is shown in Figure 7. The stress distribution is shown in Figures 8 and 9.

As seen in Figure 7, the maximum deformation occurs at the upper part of the vertical wall of the model. As seen in Figure 8, at the maximum deformation of the model, the maximum compressive stress on the outer side of the steel bar was 350 MPa, the maximum tensile stress of the inner side of the main reinforcement was 350 MPa, and the stress on the connecting steel bar was relatively low. Due to stress concentration caused by the restraint force, there were large stress distributions at both ends of the model. For the whole model, the stress on the arch was low, and the vertical wall was the weak portion of the model. As seen in Figure 9, the

Table 1: Parameters used in the ANSYS numerical model.

Materials	Peak strength (MPa)	E (MPa)	μ	Constant R
Main reinforcement	350	2.0×10^5	0.3	452.4 mm^2
Surface steel bar	350	2.0×10^5	0.3	200.9 mm^2
Connect steel bar	250	2.1×10^5	0.25	50.2 mm^2
Concrete	28.1	2.55×10^4	0.2	

Note: the shear transferring coefficient of the concrete element was 0.3 when opened and 1 when closed.

Figure 6: Numerical model.

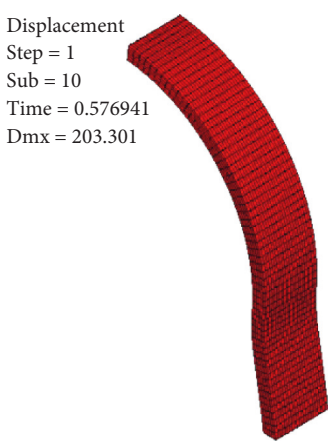

Figure 7: Deformation of the model.

tensile stress of the concrete element was low, and there were no fractures caused by tensile stress, which indicated that it was under compressive stress. The stress was mainly concentrated on the vertical wall, and the maximum compressive stress was 28.05 MPa. Overall, the inside stress on the entire structure was greater than the outside stress.

4. Analog Simulation Experiment

A comprehensive analysis of the experimental conditions and the actual condition of the north wing main haulage roadway of the Du'erping coal mine was performed. In the engineering design, the ratio of the size of the prototype to the experimental model was 2 : 1, and the material used in the model was the same as the material used in the prototype [28–31].

The parametric equation is as follows:

$$f = (\sigma, p, A, D, L, E, \gamma) = 0, \tag{12}$$

where σ is the stress in Pa, p is the normal distribution load in Pa, D is the cross-sectional area in m^2, and E is the elastic modulus in Pa.

The dimensional analysis method is used to find the similarity criterion, and the criterion form is

$$\pi = \sigma^a P^b A^c D^d L^e E^f. \tag{13}$$

By substitution, the dimension is

$$[\pi] = \left[N^0 L^0 T^0\right] = \left[NL^{-2}\right]^a [N]^b \left[L^2\right]^c \left[L^3\right]^d [L]^e \left[NL^{-2}\right]^f. \tag{14}$$

The equations have equal dimensions on both sides; therefore,

$$\begin{cases} a + b + f = 0, \\ -2a + B + 2c + 3\ d + e - 2f = 0. \end{cases} \tag{15}$$

Expressions of the similarity criterion can be finally obtained as follows:

$$\begin{aligned} \pi_1 &= \frac{\sigma}{E}, \\ \pi_2 &= \frac{P}{E}, \\ \pi_3 &= \frac{A}{L^2}, \\ \pi_4 &= \frac{D}{L^3}. \end{aligned} \tag{16}$$

4.1. Model. According to the actual condition of the north wing main haulage roadway, it was determined that the ratio of the experimental concrete in this model should be 1 : 1.84 : 1.84 : 0.45 for cement : sand : stone : water. The size of the specimen was 400 mm high, 100 mm thick, and 0.0724 m^3 in volume. The poured model was constructed in a laboratory, while a set of standard concrete specimens were poured for the strength test. Due to a long experimental loading period, to ensure strength stability and the elastic modulus of the specimens during loading, the loading experiment was performed after the curing period.

In accordance with realistic conditions, the diameter of the main reinforcement for the model was 12 mm, and the diameter of the connecting steel bar was 8 mm. Fourteen points were selected on the model, as seen in Figure 10.

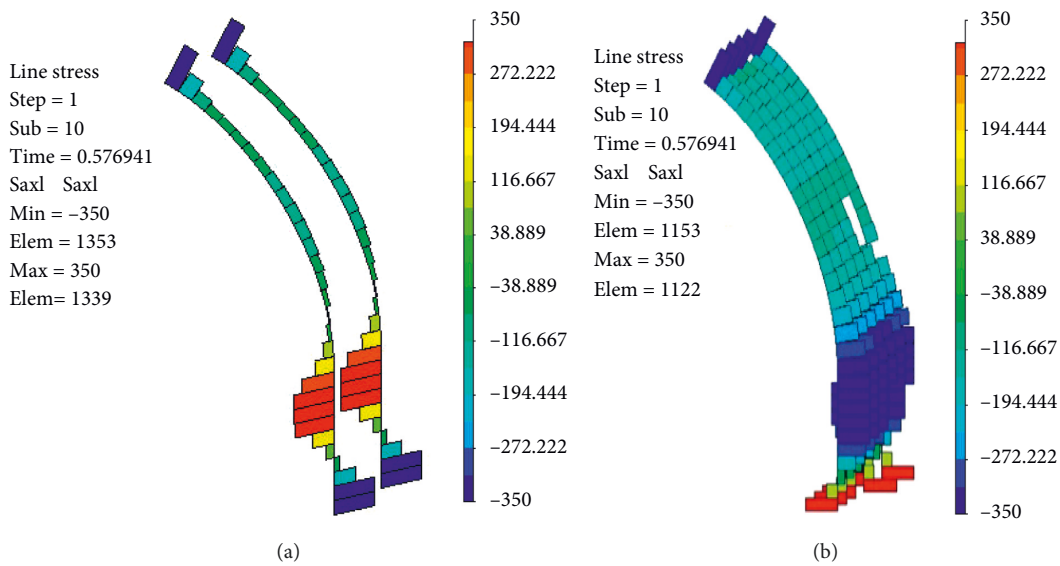

Figure 8: Stress distribution of steel bar on (a) main reinforcement and (b) surface steel bar.

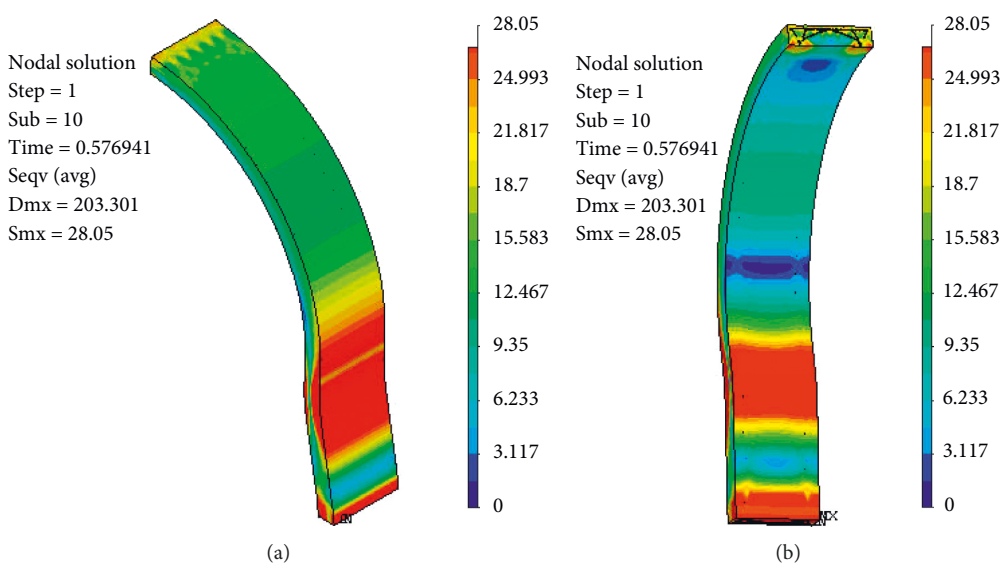

Figure 9: Stress distribution of the concrete. (a) the outer side and (b) the inner side of the concrete.

Measuring point #1 was located on the middle main reinforcement approximately one quarter of the entire length from the end. Measuring point #2 was located on the secondary reinforcement approximately one quarter of the entire length from the end. Measuring point #3 was located on the bridge frame approximately one quarter of the entire length from the end. Measuring point #4 was located on the arc bridge frame approximately one quarter of the entire length from the end. Measuring point #5 was located on the lateral connecting the steel bar approximately one quarter of the entire length from the end. Measuring point #8 was located in the middle of the symmetry plane of the middle of the main reinforcement. Measuring point #9 was located in the middle of the symmetry plane of the secondary reinforcement. Measuring point #10 was located in the middle of the symmetry plane of the bridge frame. Measuring point #11 was located in the middle of the symmetry plane of the arc bridge frame. Measuring point #12 was located in the middle of the symmetry plane of the lateral connecting steel bar. In addition, two measuring points were located in the middle and one quarter of the entire length from the end of the model's medial surface. Strain gauges were attached in two directions at every measuring point. Measuring points #6 and #13 were the vertical strain measuring points located on the medial surface of the concrete, and points #7 and #14 were the horizontal strain measuring points located on the lateral surface of the concrete.

4.2. Measuring and Loading. To simulate the load distribution, three hydraulic jacks were used, and the maximum

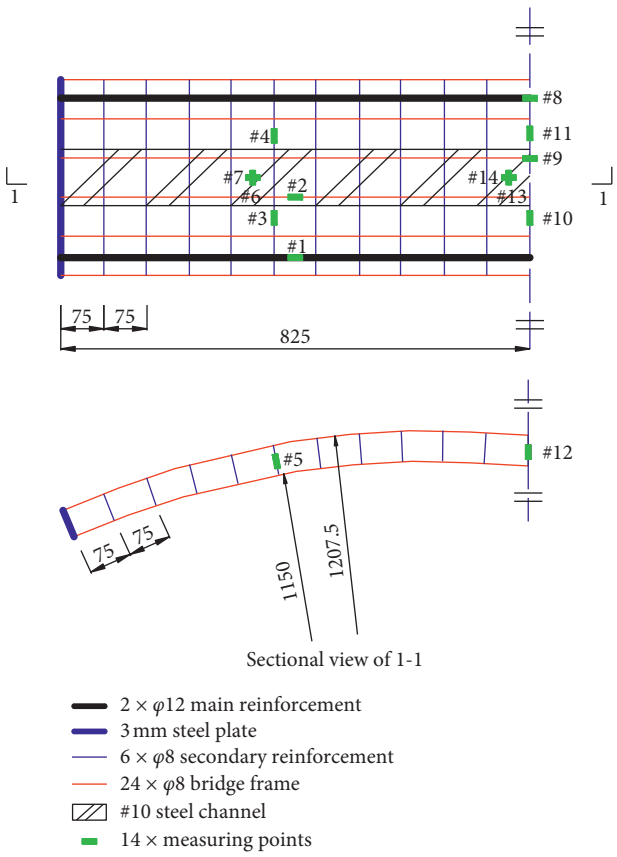

Figure 10: Arrangement of the measuring points.

pressure of each cylinder was 1000 kN. As shown in Figure 11, the thick steel plates and mortar were used to convert the point load of the jack into surface load. The two ends of the specimen were fixed with double steel plates. Grease was applied on the middle steel plate so that the specimen could slide and avoid stress concentration at both ends. The measuring equipment used high-speed static strain gauges, and the data were automatically collected by the computer. The strain gauges were divided into two groups: one group was attached to the steel bar and one group was attached to the concrete. Each group was equipped with a compensating plate. The measuring circuit used a half-bridge circuit.

According to the calibration of the cylinder, the pressure conversion relationship was determined as follows:

$$p = 32.779p_0 + 3.8929, \tag{17}$$

where p is the output pressure of cylinder in kN and p_0 is the output reading of the cylinder in MPa.

The longitudinal displacement of the model is

$$\Delta r = \bar{\varepsilon} \times r = 1.13\bar{\varepsilon} \times 10^{-3}, \tag{18}$$

where $\bar{\varepsilon}$ is the average horizontal strain and r is the inside radius of the shell in mm.

4.3. Analysis of Experimental Results. The material parameters of the concrete were determined using a standard specimen that was poured at the same time the structure was

Figure 11: Test equipment.

constructed. The results were P_{cr1} = 718 kN, P_{cr2} = 752 kN, and P_{cr3} = 687 kN, and the collapsing strength of concrete specimen was σ_c = 26.8 MPa.

After the cylinder was set to zero, it began to load at the initial pressure of 1.0 MPa and was measured every 1.0 MPa until the model failed. The ultimate bearing capacity of the support structure was 14 MPa. The measurement points were classified as follows: #1 and #8 on the main reinforcement were classified as Group 1, #2 and #9 on the secondary reinforcement were classified as Group 2, #3 and #10 on the bridge frame were classified as Group 3, #4 and #11 on the arc bridge frame were classified as Group 4, #5 and #12 on the connecting steel bar were classified as Group 5, and #6, #7, #13, and #14 located on the concrete to measure vertical strain and horizontal strain were classified as Group 6. The strain-load curves of the model are shown in Figure 12.

During the experiment, when a load of 9 MPa was applied, cracks appeared near both ends of the specimen. When a load of more than 10 MPa was applied, peeling occurred at both ends of the specimen, but there was no damage. Radial sliding occurred at the constraints of both ends. However, the entire model remained stable. With continued loading, cracks appeared mainly in the concrete layer. When a load of 14 MPa was applied, the model structure broke. The location of the broken portion was near the bearing surfaces at both ends of the shell, and the concrete was crushed. This was consistent with the results of the theoretical analysis and the numerical simulation analysis. The failure surface was an oblique section. According to the Mohr–Coulomb strength criterion, the mode of fracturing was a combination of compression and shearing. The failure state of the model is shown in Figure 13.

The ultimate bearing capacity of the model was 14 MPa. The conversion using equation (4) to engineering units was 1388 kN. As shown in Figure 12, when the load was close to the limit value, the main reinforcement and secondary reinforcement in the shell reached a yield state, and the structural damage was due to the stress concentration that occurred at both ends. To test the bearing capacity of the whole support of the "reinforced shell + shotcrete" structure, the whole "vertical wall semicircular arch reinforced shell + concrete" structure was tested. The whole structure is shown in Figure 14. The experimental support consisted of a

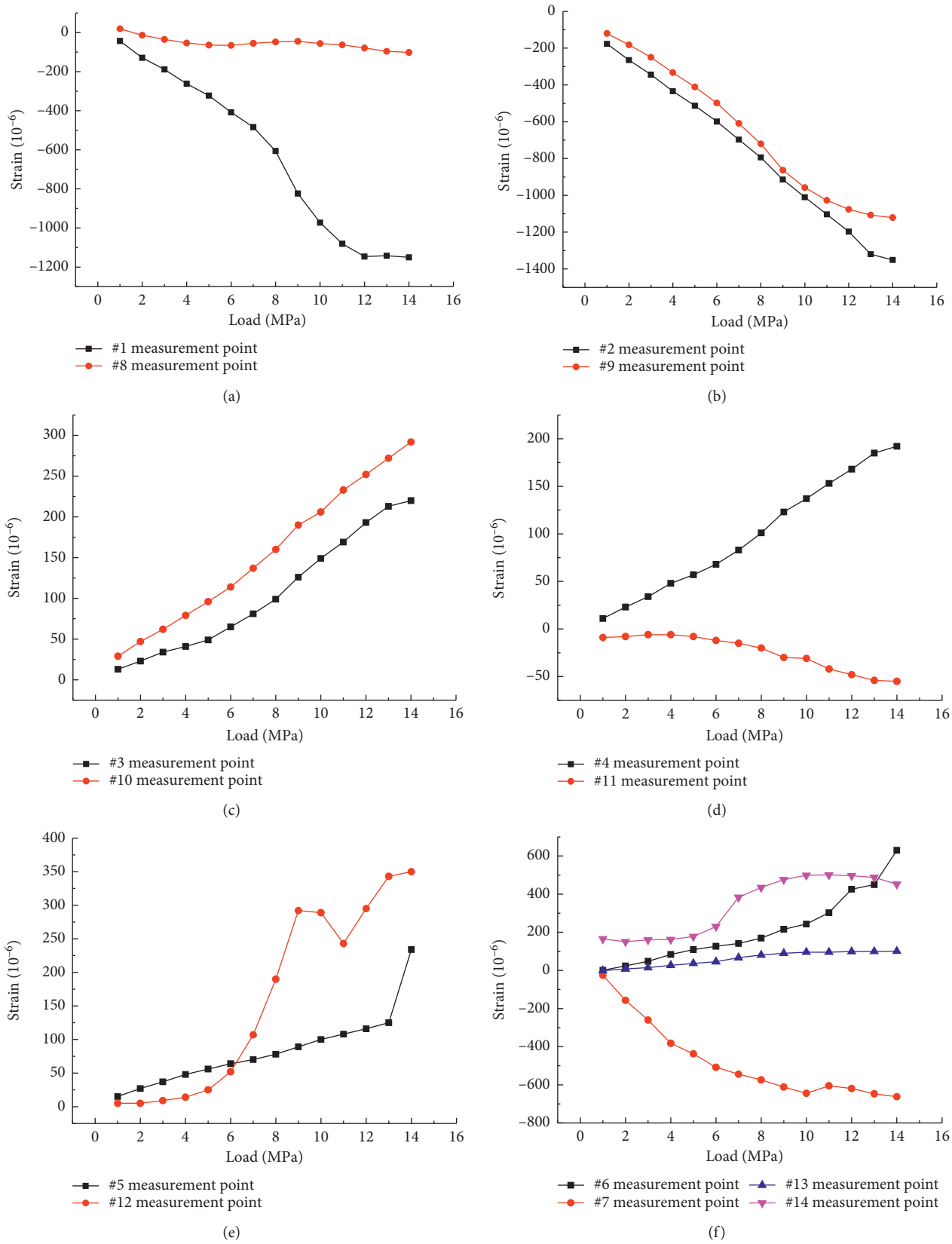

Figure 12: Strain-load curve of the model. (a) Group 1. (b) Group 2. (c) Group 3. (d) Group 4. (e) Group 5. (f) Group 6.

(a) (b)

Figure 13: Failure state of the model.

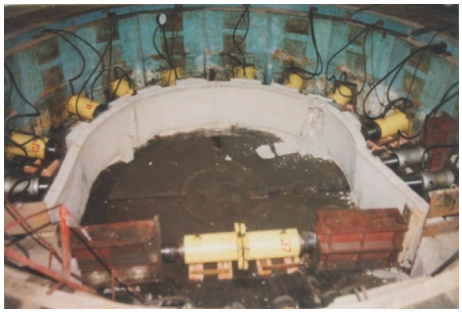

Figure 14: Set up used to test the bearing capacity of the whole supporting structure.

top arc plate and two lateral arc plates, and its structure was the same as the prototype support. A total of 14 jacks were installed along the perimeter of the support for loading purposes. The structure was supported on a concrete base, and the two walls were supported by a retractable cross brace to simulate the yielding support effect of the floor strata on the support structure. During the experiment, the jacks were loaded synchronously. The ratio of vertical wall load strength to arch load strength was controlled between 0.7 and 0.8. The stress of the steel bars and the deformation of the concrete shell were measured simultaneously.

When the total load reached 316 kN, the right vertical wall was destabilized due to large flexure fracture, and the left vertical wall began to crack, while the vault remained intact. The carrying capacity of the prototype structure can be calculated as follows:

$$C_P = C_E K = 316 \times 1.5^2 = 711\,\text{kN}, \tag{19}$$

where C_P is the carrying capacity of the prototype support in kN, C_E is the carrying capacity of the experimental support in kN, and K is the similarity ratio of the support's sectional area.

Judging from the engineering analogy, the support structure of the "vertical wall semicircular arch reinforced shell + shotcrete" was sufficient to reliably support the north wing main haulage roadway of the Du'erping coal mine.

5. Engineering Application

5.1. Support Design. Based on the numerical simulation and the analogic simulative experiment, combined with the engineering geological conditions of the Du'erping coal mine and the shape of the roadway cross section, the structure of the reinforced shell support vertical wall semicircular arch was designed. As seen in Figure 15, the reinforced shell support was divided into three sections: a top reticulated shell and two lateral reticulated shells. The structure of the reticulated shell is shown in Figure 16, and the assembled support on the ground is shown in Figure 17.

After the reinforced shell support was completed, the shotcrete filled the gaps in the reinforced shells and formed a reinforced concrete structure with high strength. Furthermore, the concrete layer would be capable of sealing fractures in the surrounding rock of the roadway. The new support structure is shown in Figure 18.

5.2. Field Monitoring. To research the support effect of the new support structure, two types of monitoring points were arranged on-site: one monitored the roadway convergence and the other monitored the surrounding rock pressure [32–35].

5.2.1. Arrangement of Monitoring Points. As seen in Figure 19(a), six measuring lines were selected to monitor the roadway convergence (a total of five measuring points: one was arranged on the vault and four were arranged on the lateral wall). As seen in Figure 19(b), three measuring points were selected to monitor the surrounding rock pressure; one was arranged on the vault, and two were arranged on the lateral wall.

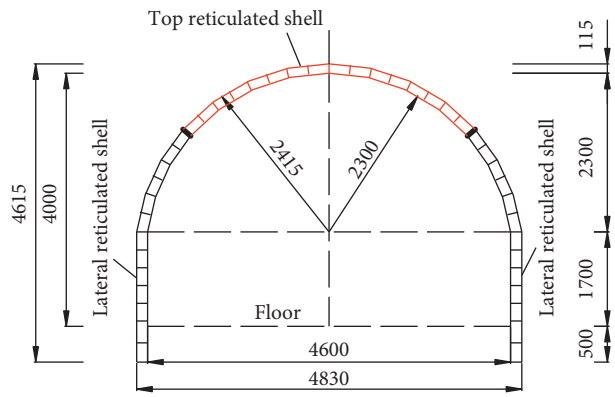

Figure 15: Reinforced shell support.

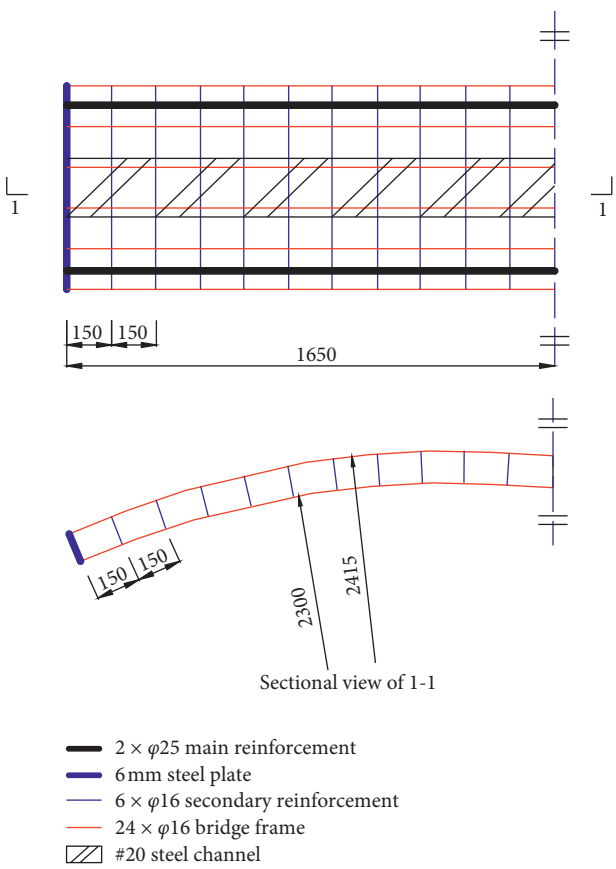

Figure 16: Structure of the reticulated shell.

5.2.2. Monitoring Results Analysis. The roadway convergence monitoring curves are shown in Figure 20, and the surrounding rock pressure measuring curve is shown in Figure 21.

As seen in Figure 20, the deformation of the roadway tended to be stable after 20 days of support, and the amount of convergence was small. The maximum convergence of the two roadway walls was 19 mm, and the maximum convergence of the vault was only 10 mm. As seen in Figure 21, the surrounding rock pressure changed significantly within

Figure 17: Assembled support.

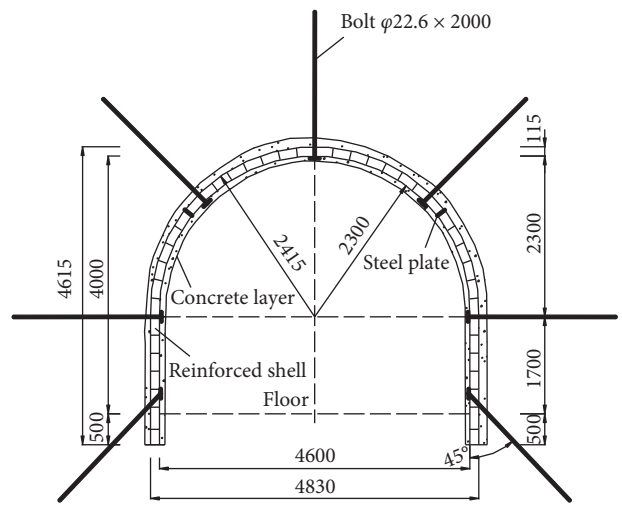

Figure 18: New support structure.

the 30 days, with the initial pressures of the two roadway walls being 0.032 MPa and 0.039 MPa, respectively, and the peak pressures reaching 0.290 MPa and 0.306 MPa, respectively. When the pressures of the two roadway walls were 0.284 MPa and 0.294 MPa, respectively, the pressure tended to be stable. The initial pressure on the rock surrounding the vault was 0.029 MPa, and the peak pressure was 0.196 MPa. When the pressure on the rock surrounding the vault was 0.19 MPa, the pressure on the rock surrounding the vault tended to be stable.

The result of the on-site monitoring showed that the "reinforced shell + bolt + shotcrete" support structure and the rock surrounding the roadway performed well. The new support structure fully withstood the bearing capacity of the surrounding rock, extended the time for self-stabilization in the surrounding rock, and significantly improved the roadway support conditions.

6. Conclusions

(1) The new support structure consisting of "reinforced shell + bolt + shotcrete" has the simultaneous advantages of flexible support and rigid support. It was developed to improve the stress state and increase support strength. The viability of this structure was

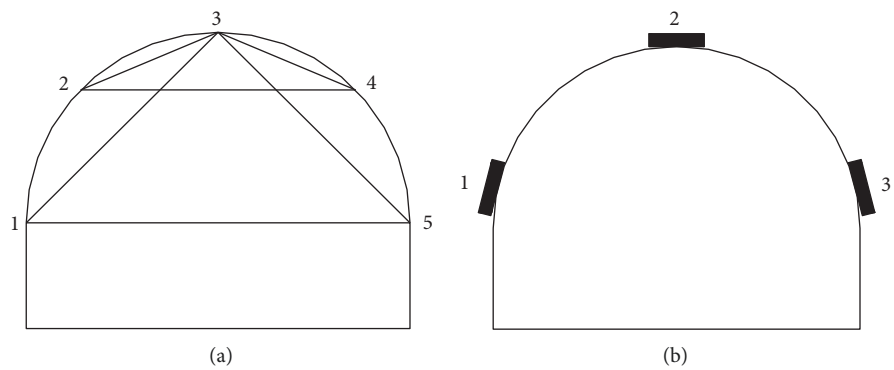

Figure 19: Arrangement of the measuring points: (a) roadway convergence and (b) surrounding rock pressure.

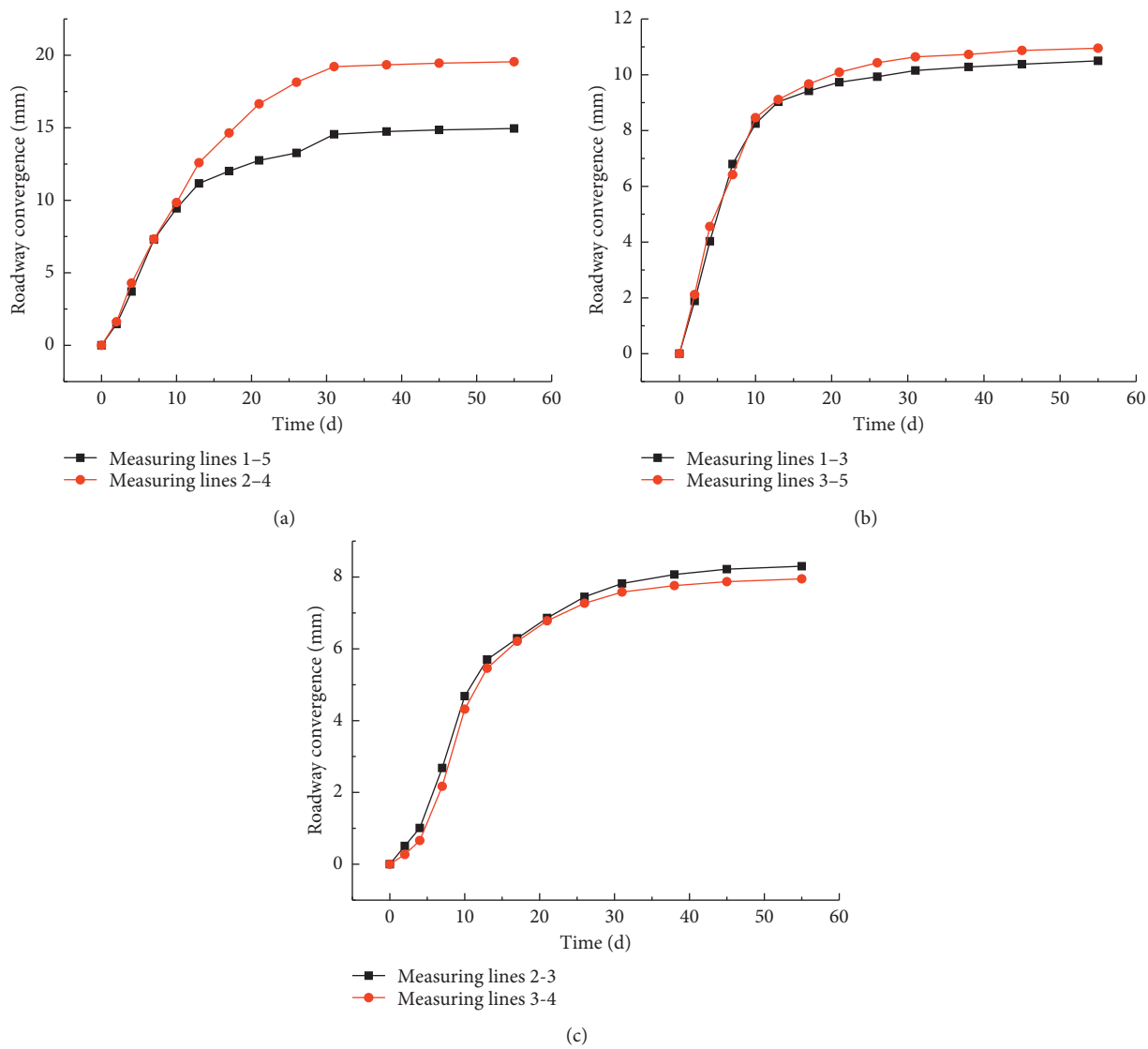

Figure 20: Roadway convergence monitoring curves of (a) lines 1–5 and lines 2–4, (b) lines 1–3 and lines 3–5, and (c) lines 2-3 and lines 3-4.

tested using field experiments, and the results demonstrated that the new support structure effectively improved roadway stability.

(2) Compared with traditional support structures, this new support design is able to control large roadway deformations caused by surrounding broken rock.

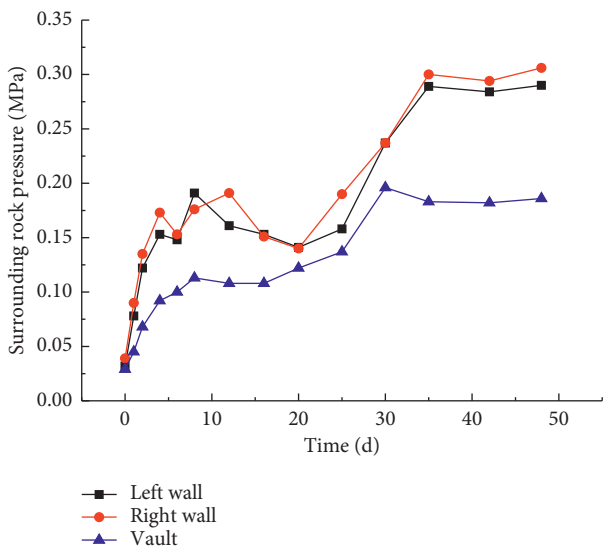

Figure 21: Surrounding rock pressure measuring curve.

The reinforced shell support is easy to install, utilizes light weight, three-dimensional continuous support, enhances stability, and is easy to construct and incorporate into projects.

(3) A comprehensive analysis of the theoretical calculations, the numerical simulations, and the analog simulation showed that the vertical wall of the reinforced shell support was the weakest part of the support. Under extremely unstable surrounding rock conditions, the vertical wall could be replaced by using a cambered wall, which would greatly improve the bearing capacity.

Data Availability

All data included in this study are available upon request by contacting the corresponding author.

Conflicts of Interest

The authors declare no conflicts of interest.

Authors' Contributions

Chaowen Hu and Xiaojie Yang were responsible for conceptualization; Chaowen Hu designed the methodology; Chaowen Hu and Yubo Zhou developed the software framework; Chaowen Hu and Jianhui Liang performed investigation; Chaowen Hu and Guofeng Ni managed data curation; and Ruifeng Huang edited the article. Xiaojie Yang and Chaowen Hu contributed equally to this work.

Acknowledgments

This work was supported by the National Natural Science Foundation of China (no. 41672347), which is gratefully acknowledged.

References

[1] H. P. Kang, J. Lin, and M. J. Fan, "Investigation on support pattern of a coal mine roadway within soft rocks—a case study," *International Journal of Coal Geology*, vol. 140, no. 2, pp. 31–40, 2015.

[2] C. Wang, Y. Wang, and S. Lu, "Deformational behaviour of roadways in soft rocks in underground coal mines and principles for stability control," *International Journal of Rock Mechanics and Mining Sciences*, vol. 37, no. 6, pp. 937–946, 2018.

[3] A. Paternesi, H. F. Schweiger, and G. Scarpelli, "Parameter calibration and numerical analysis of twin shallow tunnels," *Rock Mechanics and Rock Engineering*, vol. 50, no. 5, pp. 1243–1262, 2017.

[4] T. Bong and A. W. Stuedlein, "Effect of cone penetration conditioning on random field model parameters and impact of spatial variability on liquefaction-induced differential settlements," *Journal of Geotechnical and Geoenvironmental Engineering*, vol. 144, no. 5, article 04018018, 2018.

[5] S. Q. Duan, X. T. Feng, Q. Jiang, G. F. Liu, S. F. Pei, and Y. L. Fan, "In situ observation of failure mechanisms controlled by rock masses with weak interlayer zones in large underground cavern excavations under high geostress," *Rock Mechanics and Rock Engineering*, vol. 50, no. 9, pp. 2465–2493, 2018.

[6] X. B. Li, F. Feng, D. Y. Li, K. Du, P. G. Ranjith, and J. Rostami, "Failure characteristics of granite influenced by sample height-to-width ratios and intermediate principal stress under true-triaxial unloading conditions," *Rock Mechanics and Rock Engineering*, vol. 51, no. 5, pp. 1321–1325, 2019.

[7] Y. Chen, S. Ma, and Y. Yu, "Stability control of underground roadways subjected to stresses caused by extraction of a 10-m-thick coal seam: a case study," *Rock Mechanics and Rock Engineering*, vol. 50, no. 9, pp. 2511–2520, 2017.

[8] Y. Kang, Q. Liu, G. Gong, and H. C. Wang, "Application of a combined support system to the weak floor reinforcement in deep underground coal mine," *International Journal of Rock Mechanics and Mining Sciences*, vol. 71, no. 3, pp. 143–150, 2014.

[9] F. T. Wang, C. Zhang, S. F. Wei, X. G. Zhang, and S. H. Guo, "Whole section anchor–grouting reinforcement technology and its application in underground roadways with loose and fractured surrounding rock," *Tunnelling and Underground Space Technology*, vol. 51, no. 2, pp. 133–143, 2016.

[10] L. Chen, G. Sheng, and G. Chen, "Investigation of impact dynamics of roof bolting with passive friction control," *International Journal of Rock Mechanics and Mining Sciences*, vol. 70, no. 6, pp. 559–568, 2014.

[11] C. Wang, Y. Wang, and S. Lu, "Deformational behaviour of roadways in soft rocks in underground coal mines and principles for stability control," *International Journal of Rock Mechanics and Mining Sciences*, vol. 37, no. 6, pp. 937–946, 2000.

[12] B. Shen, "Coal mine roadway stability in soft rock: a case study," *Rock Mechanics and Rock Engineering*, vol. 47, no. 6, pp. 2225–2238, 2014.

[13] L. He, X. M. An, X. B. Zhao, Z. Y. Zhao, and J. Zhao, "Development of a unified rock bolt model in discontinuous deformation analysis," *Rock Mechanics and Rock Engineering*, vol. 51, no. 3, pp. 827–847, 2018.

[14] W.-l. Shen, J.-b. Bai, X.-y. Wang, and Y. Yu, "Response and control technology for entry loaded by mining abutment stress of a thick hard roof," *International Journal of Rock*

Mechanics and Mining Sciences, vol. 90, no. 10, pp. 26–34, 2016.

[15] X. J. Yang, E. Y. Wang, Y. J. Wang, Y. B. Gao, and P. Wang, "A study of the large deformation mechanism and control techniques for deep soft rock roadways," *Sustainability*, vol. 10, no. 4, p. 1100, 2018.

[16] Y.-Y. Jiao, L. Song, X.-Z. Wang, and A. Coffi Adoko, "Improvement of the U-shaped steel sets for supporting the roadways in loose thick coal seam," *International Journal of Rock Mechanics and Mining Sciences*, vol. 60, no. 2, pp. 19–25, 2013.

[17] Q. Wang, B. Jiang, S. C. Li et al., "Experimental studies on the mechanical properties and deformation & failure mechanism of U-type confined concrete arch centering," *Tunnelling and Underground Space Technology*, vol. 51, no. 8, pp. 20–29, 2016.

[18] W. P. Huang, Q. Yuan, Y. L. Tan et al., "An innovative support technology employing a concrete-filled steel tubular structure for a 1000-m-deep roadway in a high in situ stress field," *Tunnelling and Underground Space Technology*, vol. 73, no. 3, pp. 26–36, 2016.

[19] X. Chang, X. Luo, C. Zhu, and C. Tang, "Analysis of circular concrete-filled steel tube (CFT) support in high ground stress conditions," *Tunnelling and Underground Space Technology*, vol. 43, no. 7, pp. 41–48, 2014.

[20] W. Yu, W. Wang, X. Chen, and S. Du, "Field investigations of high stress soft surrounding rocks and deformation control," *Journal of Rock Mechanics and Geotechnical Engineering*, vol. 7, no. 4, pp. 421–433, 2015.

[21] X. Tan, W. Chen, H. Liu et al., "A combined supporting system based on foamed concrete and U-shaped steel for underground coal mine roadways undergoing large deformations," *Tunnelling and Underground Space Technology*, vol. 68, no. 9, pp. 196–210, 2017.

[22] S.-Q. Yang, M. Chen, H.-W. Jing, K.-F. Chen, and B. Meng, "A case study on large deformation failure mechanism of deep soft rock roadway in Xin'An coal mine, China," *Engineering Geology*, vol. 217, no. 1, pp. 89–101, 2017.

[23] L. Malmgren and E. Nordlund, "Behaviour of shotcrete supported rock wedges subjected to blast-induced vibrations," *International Journal of Rock Mechanics and Mining Sciences*, vol. 43, no. 4, pp. 593–615, 2006.

[24] M. R. Islam and R. Shinjo, "Numerical simulation of stress distributions and displacements around an entry roadway with igneous intrusion and potential sources of seam gas emission of the Barapukuria coal mine, NW Bangladesh," *International Journal of Coal Geology*, vol. 78, no. 4, pp. 249–262, 2009.

[25] J. Toraño, R. R. Díez, J. M. Rivas Cid, and M. M. C. Barciella, "FEM modeling of roadways driven in a fractured rock mass under a long wall influence," *Computers and Geotechnics*, vol. 29, no. 6, pp. 411–431, 2002.

[26] Z. Wen, Y. Tan, Z. Han, and F. Meng, "Construction of time-space structure model of deep stope and stability analysis," *Polish Journal of Environmental Studies*, vol. 25, no. 6, pp. 2633–2639, 2016.

[27] F. Feng, X. B. Li, J. Rostami, D. X. Peng, D. Y. Li, and K. Du, "Numerical investigation of hard rock strength and fracturing under polyaxial compression based on Mogi-Coulomb failure criterion," *International Journal of Geomechanics*, vol. 19, no. 4, article 04019005, 2019.

[28] X.-m. Sun, F. Chen, M.-c. He, W.-l. Gong, H.-c. Xu, and H. Lu, "Physical modeling of floor heave for the deep-buried roadway excavated in ten degree inclined strata using infrared thermal imaging technology," *Tunnelling and Underground Space Technology*, vol. 63, no. 3, pp. 228–243, 2017.

[29] S. C. Li, Q. Wang, H. T. Wang et al., "Model test study on surrounding rock deformation and failure mechanisms of deep roadways with thick top coal," *Tunnelling and Underground Space Technology*, vol. 47, no. 10, pp. 52–63, 2015.

[30] P. Roy, W. L. Du Frane, Y. Kanarska, and S. D. C. Walsh, "Numerical and experimental studies of particle settling in real fracture geometries," *Rock Mechanics and Rock Engineering*, vol. 49, no. 11, pp. 4557–4569, 2016.

[31] Q. Lei, J.-P. Latham, J. Xiang, C.-F. Tsang, P. Lang, and L. Guo, "Effects of geomechanical changes on the validity of a discrete fracture network representation of a realistic two-dimensional fractured rock," *International Journal of Rock Mechanics and Mining Sciences*, vol. 70, no. 9, pp. 507–523, 2014.

[32] B. Shen, A. King, and H. Guo, "Displacement, stress and seismicity in roadway roofs during mining-induced failure," *International Journal of Rock Mechanics and Mining Sciences*, vol. 45, no. 5, pp. 672–688, 2008.

[33] Q. Yao, X. Li, F. Pan, T. Wang, and G. Wang, "Deformation and failure mechanism of roadway sensitive to stress disturbance and its zonal support technology," *Shock and Vibration*, vol. 2016, Article ID 1812768, 14 pages, 2016.

[34] H. Yan, F. He, T. Yang, L. Li, S. Zhang, and J. Zhang, "The mechanism of bedding separation in roof strata overlying a roadway within a thick coal seam: a case study from the Pingshuo Coalfield, China," *Engineering Failure Analysis*, vol. 62, no. 4, pp. 75–92, 2016.

[35] N. Zhang, L. Yuan, C. Han, J. Xue, and J. Kan, "Stability and deformation of surrounding rock in pillarless gob-side entry retaining," *Safety Science*, vol. 50, no. 4, pp. 593–599, 2012.